crystals

MDPI

Article

The CeO_X and MnO_X Nanocrystals Supported on TiO_2–Graphene Oxide Catalysts and Their Selective Catalytic Reduction Properties at Low Temperature

Zhensong Tong [1,2,*], Xining Lu [3] and Cunyi Song [1,2]

1 School of Energy and Environmental Engineering, University of Science and Technology Beijing, Beijing 100083, China; hj@ustb.edu.cn
2 Beijing key laboratory of resource-oriented treatment of industrial pollutants, Beijing 100083, China
3 China Metallurgical Industry Planning and Research Institute, Beijing 100711, China; luxining@mpi1972.com
* Correspondence: tongzhensong@163.com; Tel.: +86-010-6233-3434

Academic Editors: Roberto Comparelli, Lucia Curri and Marinella Striccoli
Received: 23 February 2017; Accepted: 29 May 2017; Published: 2 June 2017

Abstract: A series of 9%CeO_x–MnO_x/TiO_2–GO nanocomposites with different molar ratios of Ce/Mn were synthesized by the sol-gel and ultrasonic impregnation methods and characterized by field emission scanning electron microscope (FESEM), high resolution transmission electron microscopy (HRTEM), N_2 adsorption (BET) analysis, X-ray photoelectron spectroscopy (XPS), and Fourier transform infrared spectroscopy (FT–IR). The results showed that various valences of Ce and Mn oxides were uniformly distributed on the surface of TiO_2–GO multilayered supports. The coexistence of various valences of Ce and Mn oxides can improve the redox performance of the catalyst. With the introduction of Ce, the amount of MnO_2 and non-stoichiometric MnO_x/Mn, the total oxygen and chemisorbed oxygen content, and the electron transfer ability of the catalyst increased significantly. When the molar ratio of Ce/Mn was 0.3, the catalysts exhibited high selective catalytic reduction activity (more than 99% at 180 °C) and N_2 selectivity. The presence of hydrophilic groups on the surface of the GO was considered as the critical factor influencing the H_2O resistance of the catalyst. Due to the pre-sulfuring process of GO, serious sulfation of the active component can be prevented, and the catalyst exhibited excellent SO_2 resistance.

Keywords: nanocrystal; selective catalytic reduction; graphene oxide; cerium oxides; manganese oxides

1. Introduction

Removal of the nitrogen oxides (NO_x) emitted from the combustion of fossil fuels has attracted much more attention worldwide because NO_x can cause acid rain, photochemical smog, greenhouse effects, and damage to human health [1,2]. Currently, low-temperature selective catalytic reduction (SCR) has been considered as a reasonable and effective strategy to decrease the NO_x levels in gaseous emissions [3–6].

For their relatively high activities for low-temperature NH_3-SCR, Mn-based catalysts have attracted increasing attention. It has been shown that the reaction activity of manganese oxide is affected by several factors, such as Mn oxidation state, crystallinity, specific surface area, and morphology [7–10]. However, the selective catalytic reduction (SCR) activity of MnO_x is not as high as expected, and the resistance of MnO_x to SO_2 and/or H_2O is relatively poor, so some other metal oxides are often added, such as CeO_x [11], FeO_x [12], NbO_x [13], SnO_x [14], and ZrO_x [15]. Compared with other metal oxides, CeO_x is considered more effective. The redox shift between Ce^{4+} and Ce^{3+} will result in the increase in the oxygen storage capability of MnO_x and the oxygen migration speed, which are important for the reaction activity of the catalyst [16,17]. Additionally, it has also been shown that when CeO_x is added into MnO_x, the Mn ions will enter the CeO_2 lattice to form a nanoscale solid solution [18]. On the other hand, the addition of CeO_2 can improve the distribution status of MnO_x on the surface of the support and enhance the oxidation of NO to NO_2, producing more absorbed NO_3^- on the catalyst surface, which is then reduced into N_2 by NH_3. These behaviors account for the promoting effect of CeO_2 on the SCR activity [19]. Qi et al. prepared a CeO_2–MnO_x catalyst and showed that the addition of Mn into the Ce lattice significantly improves NO conversion; however, increasing the Mn content beyond a certain point degrades this conversion [20,21]. It has also been proven that the introduction of CeO_x is beneficial to the SO_2 resistance of the catalysts. Jin et al. reported that the introduction of Ce can not only lessen the sulfation of MnO_x, but also reduce thermal stabilities of the sulfate species covered on the catalyst surface [22]. Wu et al. prepared Mn/TiO_2 and ceria-modified Mn/TiO_2 catalysts by the sol-gel method, and the results showed that the doping of ceria can prevent the formation of $Ti(SO_4)_2$ and $Mn(SO_4)_x$, and the depositions of $(NH_4)_2SO_4$ and NH_4HSO_4 can also be significantly inhibited [23].

Carbon materials, such as activated carbon (AC), AC fiber (ACF), carbon nanotubes (CNTs), ordered mesoporous carbons, graphene, and graphene oxide (GO), are considered as ideal supports of catalysts for their large specific surface areas and relatively high chemical stabilities [24–32]. GO, as the derivative of graphene, consists of a hexagonal ring-based carbon network with both sp^2 and sp^3 hybridized carbon atoms [33], both sides are accessible [34], and GO is a sheet-shaped material with large specific surface area up to 400–1500 m^2/g [35,36]. It has also been reported that the existence of extensive reactive oxygen functional groups [37–39], holes [40], carbon vacancies, and defects on the surface of GO can introduce chemically-active sites during catalysis [41]. It has been suggested that GO could be an ideal support for the growth of functional nanoparticles and would render them electrically conductive, highly dispersive, and catalytically active [35].

We recently found that MnO_x/TiO_2–GO catalysts exhibited high NH_3–SCR activity and N_2 selectivity at low temperature. The results showed that the 9%MnO_x/TiO_2–0.8%GO catalyst had the highest activity at low temperature [42]. In order to improve the SCR activity further, a certain amount of CeO_x was added to the MnO_x/TiO_2–GO catalyst in this work, which was represented as 9%Ce–Mn/TiO_2–0.8%GO. The composite catalysts were characterized by field emission scanning electron microscope (FESEM), high resolution transmission electron microscopy (HRTEM), N_2 adsorption (BET) analysis, X–ray photoelectron spectroscopy (XPS), and Fourier transform infrared spectroscopy (FT–IR), temperature-programmed desorption of NH_3(NH_3–TPD), and temperature-programmed reduction of H_2(H_2–TPR). The focus of the work was to identify the effect of the introduction of Ce and the synergistic effect of Ce, Mn, and GO on the catalytic performance of the nanocomposites. The influences of the catalyst SCR activity by H_2O and SO_2 were also determined.

2. Results and Discussion

2.1. SCR Activity of Different Molar Ratios of Ce/Mn

The SCR activities of 9%Ce–Mn/TiO_2–0.8%GO with different molar ratios of Ce/Mn at low temperature are shown in Figure 1.

From Figure 1, it can be found that the NO_x conversion efficiencies of all catalysts increased with the reaction temperature and, with the addition of Ce, the 9%Ce–Mn/TiO_2–0.8%GO catalysts exhibited higher SCR activity than that of 9%Mn/TiO_2–0.8%GO. When the Ce/Mn ratio was below 0.4, the NO_x conversion of 9%Ce–Mn/TiO_2–0.8%GO catalysts increased with the Ce/Mn ratio. When the ratio was 0.3, the catalytic activity had the highest value of 99% at 180 °C. That meant that the introduction of a certain amount of Ce was beneficial to the increase of reaction activity of the catalyst, which will be explained by the following HRTEM and XPS analyses. It can also be observed that when the Ce/Mn ratio was as high as 0.4, the efficiency decreased. Similar results have been obtained in our previous work [43]. This may be attributed to the aggregation of active components on the surface of the support, which will be interpreted by the following BET analysis.

N_2 selectivity and N_2O formation of the catalysts with the reaction temperature are shown in Figure 2. It can be found that high N_2 selectivity (>97%) and a small amount of N_2O formation (less than 10 ppm) exists over all of the catalysts. However, the addition of Ce and the increase of temperature had negative effect on the N_2 selectivity and N_2O formation of the catalysts. With the increase of the reaction temperature, much more NH_3, which acted as a reducing agent in the SCR reaction, will be oxidized to generate N_2O. As a result, the N_2 selectivity of the catalyst decreased with temperature. It has also been proven by Liu et al. that with the increase the ratio of Ce/Mn, much more N_2O will be generated. According to the definition of N_2 selectivity in Equation (2) mentioned below, the N_2 selectivity was decreased [16]. For practical application, the catalyst with reasonable molar ratios of Ce/Mn (0.3) can be chosen as a candidate for its high SCR activity, N_2 selectivity, and trace amount of N_2O formation at low temperature.

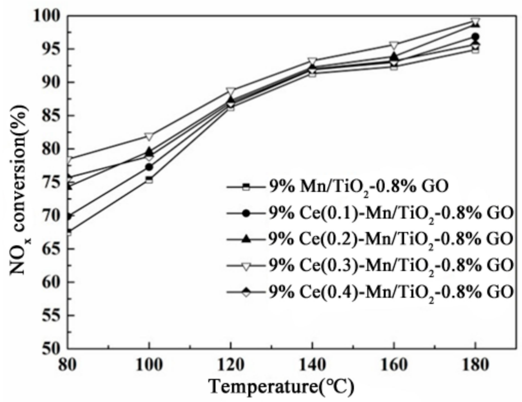

Figure 1. Low-temperature catalytic activities of MnO_x/TiO_2–0.8%GO and CeO_x–MnO_x/TiO_2–0.8%GO catalysts.

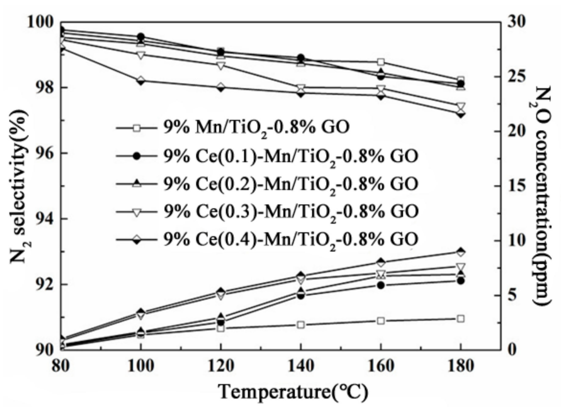

Figure 2. N_2 selectivity and N_2O formation over MnO_x/TiO_2–0.8%GO and CeO_x–MnO_x/TiO_2–0.8%GO catalysts.

2.2. Characterization of the Catalysts

2.2.1. FESEM of the Supports

FESEM images of GO and TiO_2–0.8%GO supports are shown in Figure 3a,b, respectively. From Figure 3a, the multilayer morphology of GO sheets can be observed clearly, which was considered as an ideal structure to provide a high specific surface area and prevent the aggregation of metal oxides on its surface. In Figure 3b, some white anatase TiO_2 particles could be observed distributed on the

GO surface, and there was an accumulation of them in some areas of the GO, which will be proven by the following HRTEM analysis. It has been identified that the TiO_2–0.8%GO is an ideal support for catalysts [42].

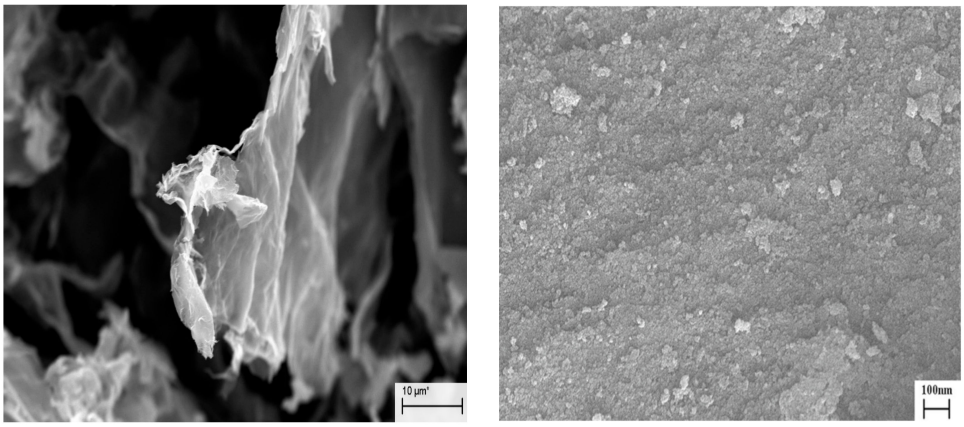

(**a**) (**b**)

Figure 3. FESEM images of (**a**) GO and (**b**) TiO_2–0.8%GO.

2.2.2. HRTEM of the Catalyst

The microstructure of 9%Ce(0.3)–Mn/TiO_2–0.8%GO was characterized by TEM and HRTEM, as shown in Figure 4b, respectively. In Figure 4a, the sheet-like morphology of GO can be observed, and the TiO_2, MnO_x, and CeO_x nanoparticles were dispersed randomly on the surface of the GO sheets. Though there was a little aggregation in some area of GO, it was not serious, which may be attributed to the introduction of GO. The corresponding HRTEM image of the catalyst was shown in Figure 4b. The observed spacing between the lattice planes of the catalyst was around 0.218, 0.352, 0.384, 0.420, 0.436, and 0.610 nm, corresponding to the (510) crystallographic planes of Ce_2O_3, the (101) crystallographic planes of anatase TiO_2, the (211) crystallographic planes of Mn_2O_3, the (110) crystallographic planes of CeO_2, the (021) crystallographic planes of Mn_3O_4, and the (001) crystallographic planes of GO, respectively. The well-distributed status of active components on the surface of the support [44] and the coexistence of multivalent metal oxides [43] can improve the selective catalytic reduction abilities of the composite catalysts at low temperature.

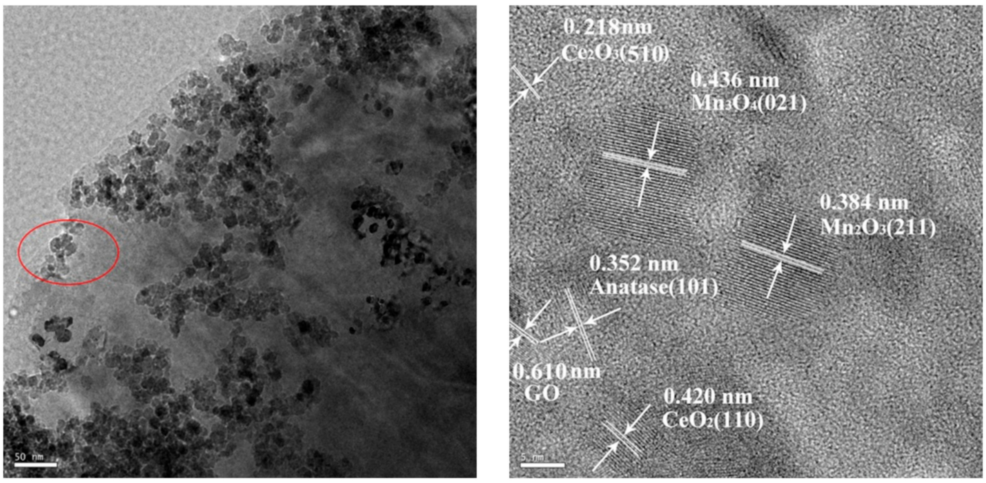

(**a**) (**b**)

Figure 4. TEM (**a**) and HRTEM image (**b**) of 9%Ce(0.3)–Mn/TiO_2–0.8%GO.

2.2.3. BET Surface Areas and Pore Size Distributions

The specific surface area, pore volume, and pore size of the CeO_x-MnO_x/TiO_2–GO and MnO_x/TiO_2–GO are summarized in Table 1. It can be found that the addition of CeO_x to the 9%Mn/TiO_2–0.8%GO had a negative effect on the specific surface area and the porous structure parameters, which has also been proven by some other analogous research [19,45,46]. When the ratio was no more than 0.3, this tendency was not very obvious, but when the Ce/Mn molar ratio reached 0.4, the specific surface area and total pore volume of the catalysts decreased significantly. For the SCR activity of 9%Ce(0.4)–Mn/TiO_2–0.8%, GO was lower than that of 9%Ce(0.3)–Mn/TiO_2–0.8%GO, and it can be concluded that the specific surface area and total pore volume of the catalyst had an effect on the reaction activity of the catalyst. On the other hand, though the 9%Ce(0.3)–Mn/TiO_2–0.8%GO had the highest activity among the catalysts, its specific area and pore volume did not have the highest value. This meant that the activity of the catalyst was affected by not only the specific surface area and total pore volume of the catalyst, but also some other important factors, which will be revealed by the following character results.

Table 1. Structural parameters of CeO_x-MnO_x/TiO_2–0.8%GO catalysts.

Catalyst	SBET	Pore Volume (cm^3/g)	Average Pore Size (nm)
9%Mn/TiO_2–0.8%GO	149	30.48	9.0
9%Ce(0.1)–Mn/TiO_2–0.8%GO	144	29.98	9.1
9%Ce(0.2)–Mn/TiO_2–0.8%GO	138	29.12	9.2
9%Ce(0.3)–Mn/TiO_2–0.8%GO	136	29.13	9.1
9%Ce(0.4)–Mn/TiO_2–0.8%GO	127	25.56	11.5

2.2.4. XPS Characterization

The atomic concentration and element chemical state on the surface of the 9%Mn/$TiO_2$0.8%GO and 9%Ce(0.3)Mn/TiO_2–0.8%GO catalysts were further investigated by XPS. Figure 5a–c illustrate the obtained XPS spectra for Mn2p, Ce3d, and O1s, respectively, and the corresponding surface atomic concentrations and relative percentages of various oxidation states are summarized in Table 2.

From Figure 5a, it can be found that the Mn 2p3/2 spectra for the 9%Mn/TiO_2–0.8%GO and 9%Ce(0.3)–Mn/TiO_2–0.8%GO catalysts can both be divided into three characteristic peaks attributed to MnO (640.9 eV), Mn_2O_3 (642.2 eV), and MnO_2 (644.6 eV). However, the bonding energy of the Mn 2p3/2 spectra in 9%Ce(0.3)–Mn/TiO_2–0.8%GO showed a slight offset toward the high value, which indicated that the electron transferability could be improved by addition of Ce [43]. The Mn 2p1/2 spectra of 9%Ce(0.3)–Mn/TiO_2–0.8%GO catalyst exhibited two characteristic peaks at 653.0 eV (MnO_x/Mn) and 654.1 eV (MnO_2), but for the Mn 2p1/2 spectra of the 9%Mn/TiO_2–0.8%GO catalyst, there was only one peak corresponding to the existence of non-stoichiometric MnO_x/Mn. The contents of Mn with different vacancies in Table 2 were achieved by calculating the percentage of the corresponding peak area. According to Table 2, the content of MnO_2 for 9%Ce(0.3)–Mn/TiO_2–0.8%GO was higher than that of 9%Mn/TiO_2–0.8%GO. This meant the introduction of Ce can increase the content of MnO_2 in the catalyst. It has been reported that MnO_2 had the highest low-temperature NH_3–SCR activity among various manganese oxides [47]. In addition, from Table 2, it is also shown that, compared with 9%Mn/TiO_2–0.8%GO catalyst, 9%Ce(0.3)–Mn/TiO_2–0.8%GO nanocomposite had a higher content of the non-stoichiometric MnO_x/Mn, which has been demonstrated to be beneficial to the redox reaction of the catalyst and further increase the removal rate of NO_x in the SCR reaction [48]. Thus, with the addition of Ce, the content of MnO_2 and non-stoichiometric MnO_x/Mn will be increased, which results in the improvement of the catalytic activity of the nanocomposite catalyst [49–51].

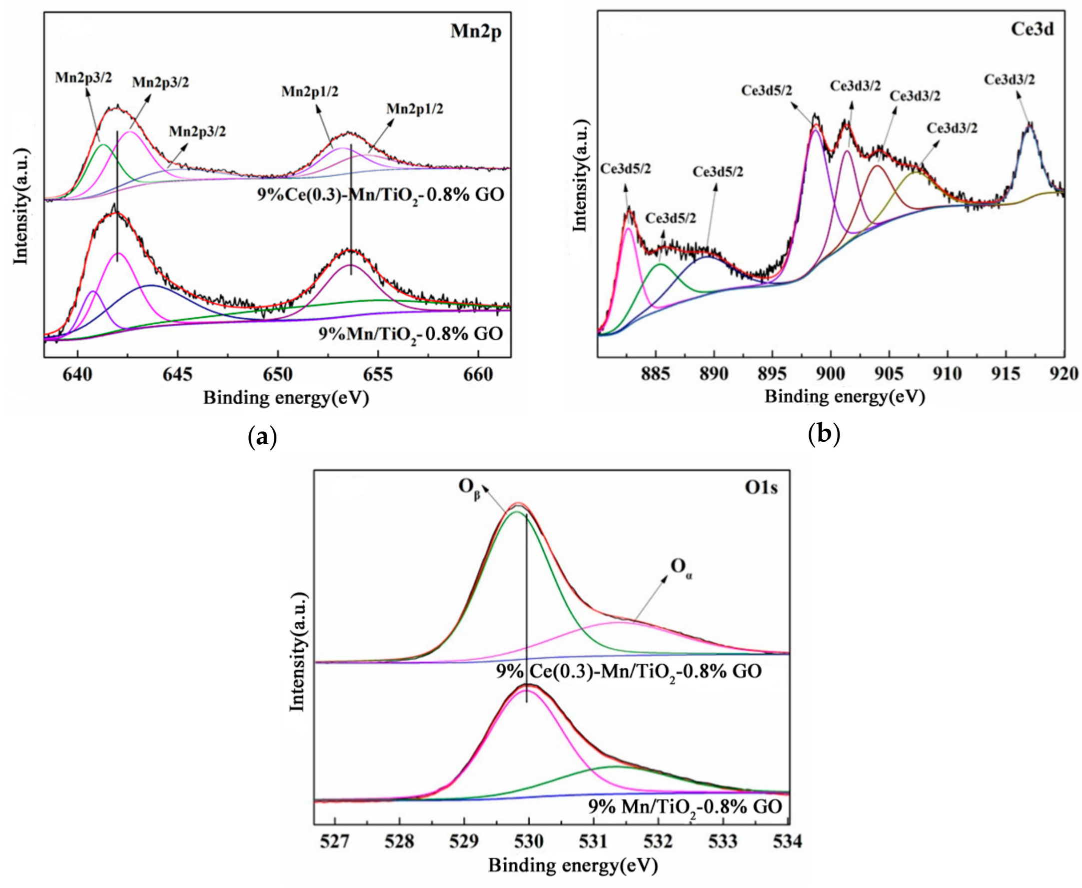

(**a**) (**b**) (**c**)

Figure 5. XPS spectra of Mn 2p (**a**), Ce 3d (**b**), and O 1s (**c**) for 9%Mn/TiO_2–0.8%GO and 9%Ce(0.3)–Mn/TiO_2–0.8%GO catalysts.

Table 2. Structural parameters of $CeO_{x-}MnO_x/TiO_2$–0.8%GO catalysts.

Catalyst	Atomic Composition (%)										
	C	Ce	Mn	Ti	O	O		Mn			
						O_α	O_β	MnO	MnO_2	Mn_2O_3	MnO_x/Mn
9%Mn/TiO_2–0.8%GO	19.45	-	5.21	21.36	53.98	17.93	36.05	1.58	1.29	1.24	1.10
9%Ce(0.3)–Mn/TiO_2–0.8%GO	16.91	3.85	4.61	17.59	57.04	15.99	41.05	1.03	1.62	0.65	1.31

The Ce3d spectrum of the 9%Ce(0.3)–Mn/TiO_2–0.8%GO catalyst, which is composed of the Ce 3d3/2 and Ce 3d5/2 spectra, are presented in Figure 5b. The Ce 3dp5/2 spectra can be divided into four characteristic peaks at 882.5 eV (Ce^{4+}), 885.8 eV (Ce^{3+}), 888.8 eV (Ce^{3+}), and 898.3 eV (Ce^{2+}), respectively, while the Ce3d3/2 spectra can also be divided into four characteristic peaks at 901.4 eV (Ce^{4+}), 903.8 eV (Ce^{3+}), 907.3 eV (Ce^{4+}), and 916.8 eV (Ce^{4+}), respectively. The coexistence of Ce^{2+}, Ce^{3+}, and Ce^{4+} can create a charge imbalance, vacancies, and unsaturated chemical bonds on the catalyst's surface [52] and, as a result, can increase the SCR activity of the catalyst [53]. Among these cerium oxides, CeO_2 has been proven as the most effective oxide type of cerium for SCR activity, which was the main valence state in the 9%Ce(0.3)–Mn/TiO_2–0.8%GO catalyst.

From Figure 5c, it can be observed that there are two types of surface oxygen in the XPS patterns of O1s for 9%Mn/TiO_2–0.8%GO and 9%Ce(0.3)–Mn/TiO_2–0.8%GO catalysts, lattice oxygen (O_β) at 529.4–530.0 eV and chemisorbed oxygen (O_α) at 531.3–531.7 eV, respectively. The chemisorbed oxygen, with higher mobility than lattice oxygen (O_β), was mainly shown as ${O_2}^{2-}$ or O^-, in the form of hydroxyl, OH^-, carbonate, and ${CO_3}^{2-}$ [54]. In Table 2, from the comparison between

9%Mn/TiO_2–0.8%GO and 9% Ce(0.3)–Mn/TiO_2–0.8%GO catalysts, it was very clear that, with the loading of Ce, the total oxygen and chemisorbed oxygen content of the catalyst increased, which implied that the catalyst would have high SCR activity at low temperature.

2.3. Resistance to H_2O and SO_2

Figure 6a–c show the resistance property of the nanocomposite catalyst to H_2O, SO_2, and H_2O+SO_2 at 180 °C. When only 10 vol % H_2O was added to the reaction system, the denitrification efficiency decreased from about 99% to 90% with the reaction time. The water in the flue gas may cause serious deactivation of the catalyst because of the competitive adsorption with NH_3 on the active sites over the catalyst surface [55]. However, when the H_2O feed was stopped, the NO_x conversion of the catalyst nearly completely recovered to the original levels. Due to the presence of hydrophilic groups on the surface of the GO sheets, the water in the flue gas can be absorbed easily, which resulted in the competitive adsorption with NH_3. Consequently, the SCR activity of the catalyst decreased obviously with the feeding of H_2O.

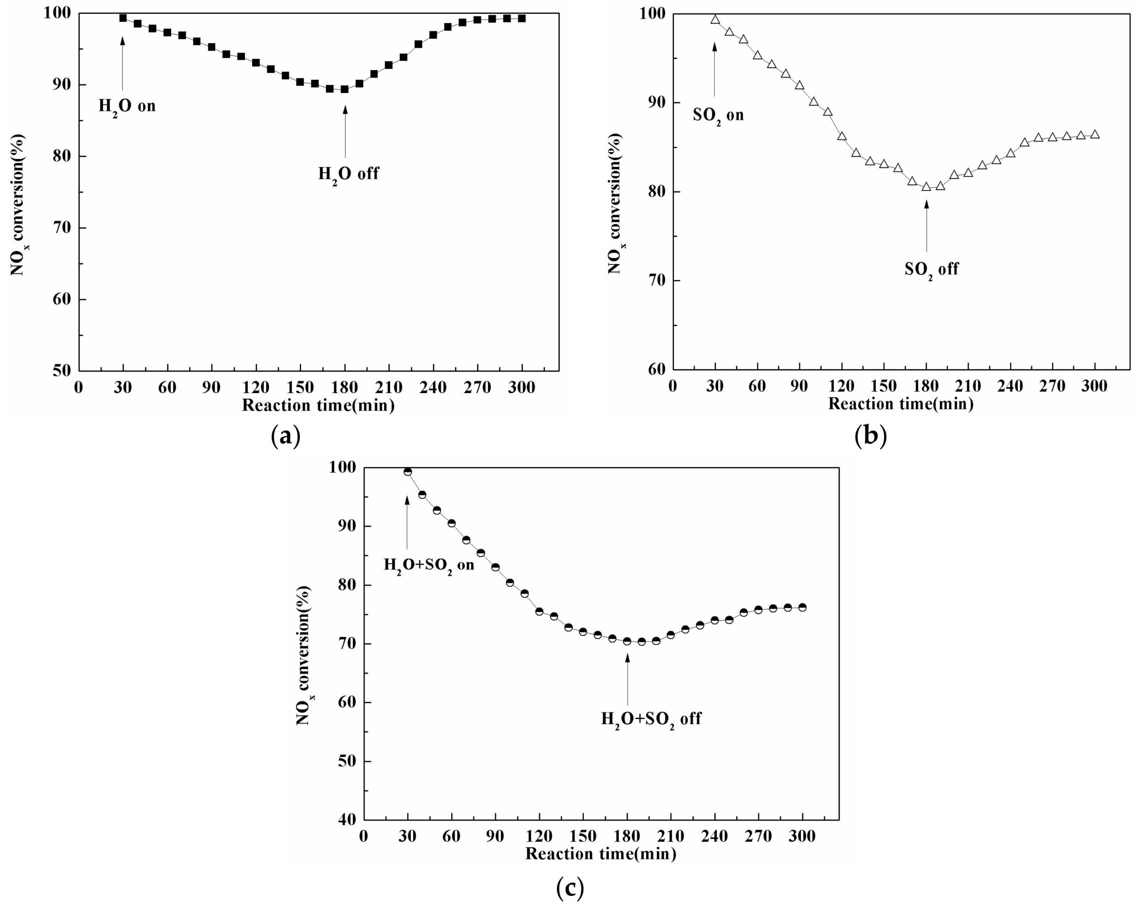

Figure 6. Effect of (**a**) H_2O, (**b**) SO_2, and (**c**) H_2O+SO_2 on NO_x conversion over 9%Ce(0.3)–Mn/TiO_2–0.8%GO catalyst.

When only 200 ppm SO_2 was fed into the reaction system, there was also a decline in the catalytic activity from 99% to a relatively high value of about 82% with time, as shown in Figure 6b. The deactivation of the catalyst caused by SO_2 is mainly attributed to the reaction between SO_2 and NH_3, active components of the catalyst. When the SO_2 feeding ceased, the conversion was restored to around 87%. As the addition of Ce can prevent the formation of manganese sulfate on the catalyst surface [22], the 9% Ce(0.3)–Mn/TiO_2–0.8%GO catalyst exhibited high resistance to the SO_2 pollutants.

When 10 vol % H_2O and 200 ppm SO_2 were added together into the SCR system, a much more serious decline in the catalytic activity from 99% to about 70% would occur. This meant there was a synergistic effect of the H_2O and SO_2 on the activation of the catalyst. When H_2O and SO_2 were removed from the system, the efficiency recovered to around 78%. In order to identify the mechanism of the deactivation of the catalyst caused by H_2O and SO_2, the FT–IR spectra of GO and TiO_2–0.8%GO support, and the fresh and poisoned 9%Ce(0.3)–Mn/TiO_2–0.8%GO catalyst were studied, as shown in Figure 7a,b, respectively.

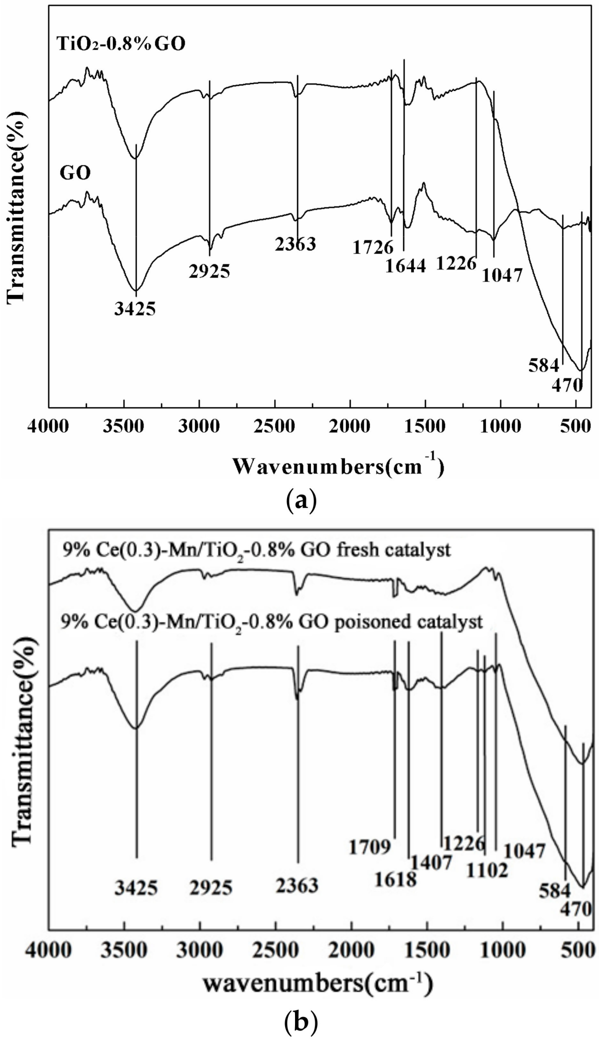

Figure 7. FT–IR spectra of (**a**) fresh and poisoned 9%Ce(0.3)–Mn/TiO_2–0.8%GO catalyst and (**b**) GO and TiO_2–0.8%GO support.

In Figure 7a, for GO and TiO_2–0.8%GO support, the peak at 3425 cm^{-1} corresponded to the −OH vibrations, and the vibration at 2925 cm^{-1} was ascribed to the aliphatic stretching vibration of molecule residues of the synthesis. The peaks at 1726 cm^{-1} and 1644 cm^{-1} were attributed to the stretching vibration of C=O bond and the C=C stretching of the Csp^2 network of GO, while the signals at 1226 cm^{-1} could be also ascribed to C–N groups originating from the catalyst synthesis [56–58]. For the TiO_2–0.8%GO support, there was a new peak at 470 cm^{-1}, which was attributed to the stretching vibration of Ti–O.

Compared the FT-IR spectra of the poisoned 9% Ce(0.3)–Mn/TiO_2−0.8%GO catalyst with that of fresh catalyst and TiO_2–0.8%GO support, it can be found that there was no obvious difference of the appearance of the character peaks. However, it can be found that the band intensity at 3425 cm^{-1} of the poisoned catalyst was larger than that of fresh catalyst, which indicated the H_2O in the flue gas poisoned the catalyst during the SCR reaction process because of the hydrophilic character of GO. It can also be observed that, for the poisoned catalyst, the band intensity of the peak at 1407 cm^{-1} was higher than that of fresh catalyst and the support. This difference implied the generation of $(NH_4)_2SO_4$ on the Lewis acid sites. This can also be demonstrated by the analysis of the peak at 1102 cm^{-1}. The peak at 1102 cm^{-1} corresponded to the existence of SO_4^{2-}, which can be observed only in the poisoned catalyst. For a large amount of concentrated sulfuric acid used in the synthesis process of GO, some SO_4^{2-} would be loaded on the surface of GO at the pre-sulfuring step. However, the band intensity at 1102 cm^{-1} for the poisoned catalyst was only slightly larger than that of fresh catalyst, which indicated the slight poisoning of SO_2 to the catalyst. Thus, it can be concluded that for the pre-sulfuring process of GO, serious sulfation of the active component can be prevented and the catalyst exhibited excellent SO_2 resistance.

2.4. NH_3-TPD Analysis

The surface acidity is an important aspect of the NH_3–SCR reaction. By using NH_3–TPD analysis, the surface acidity of 9% Mn/TiO_2–0.8%GO and 9% Ce(0.3)–Mn/TiO_2–0.8%GO catalysts were determined, and the results are presented in Figure 8.

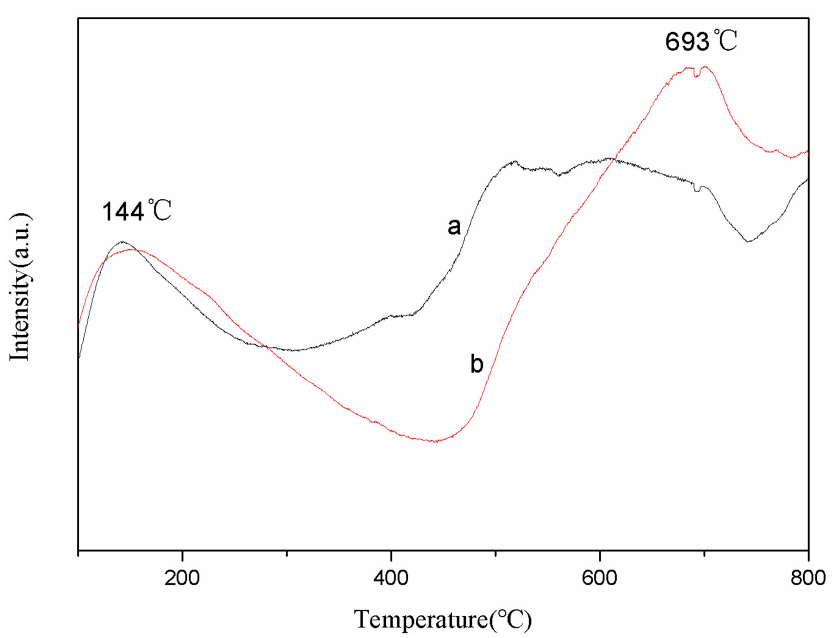

Figure 8. NH_3–TPD patterns of 9% Mn/TiO_2–0.8%GO (**a**) and 9% Ce(0.3)×Mn/TiO_2–0.8%GO (**b**).

For the NH_3–TPD pattern of 9% Mn/TiO_2–0.8%GO and 9% Ce(0.3)–Mn/TiO_2–0.8%GO, there was a strong peak at about 144 °C. For the thermal stability, the NH_3 molecules that coordinated to the Lewis acid sites was higher than that of the NH_4^+ ions bound to the Brønsted acid sites, and the desorption peak at low temperature (below 200 °C) was assigned to NH_4^+ ions bound to Brønsted acid sites [59]. It was clear that the peak area of 9% Ce(0.3)–Mn/TiO_2–0.8%GO was much larger than that of 9% Mn/TiO_2–0.8%GO, which indicated that the 9% Ce(0.3)–Mn/TiO_2–0.8%GO catalyst provided more Brønsted acidic sites than that of the 9% Mn/TiO_2–0.8%GO. Thus, the introduction of CeO_x had a significant influence on promoting NH_3 adsorption at Brønsted acidic sites. For the 9% Mn/TiO_2–0.8%GO catalyst, there was a broad peak in the temperature range of about 450–700 °C, and for 9% Ce(0.3)–Mn/TiO_2–0.8%GO there was a peak at about 693 °C. The peaks at high temperature ranging from 400–550 °C were associated with coordinated NH_3 molecules originating from the Lewis acid sites, which may originate from the decomposition of nitrite-nitrate species which are formed from the oxidation of ammonia by MnO_2 [60]. The desorption peak above 600 °C may be related to the hydroxyl groups on the surface [61]. It has been proven that the Brønsted acid sites also have an important role in the SCR reaction [62], which may be one of the reasons that the SCR reaction activity of 9% Ce(0.3)–Mn/TiO_2–0.8%GO was higher than that of 9% Mn/TiO_2–0.8%GO.

2.5. H_2-TPR Analysis

H_2-TPR is a valid method to determine the redox performance of the catalyst. Figure 9 shows the TPR curves of the catalysts. It can be found that the H_2-TPR pattern of 9% Mn/TiO_2–0.8%GO and 9% Ce(0.3)–Mn/TiO_2–0.8%GO was similar, where there was a strong peak at about 446 °C. This peak was attributed to reduction from MnO_2 to Mn_2O_3 [63]. However, it was obvious that the peak area of 9% Ce(0.3)–Mn/TiO_2–0.8%GO was much larger than that of 9% Mn/TiO_2–0.8%GO, which meant that 9% Ce(0.3)–Mn/TiO_2–0.8%GO had larger H_2 consumption than that of 9% Mn/TiO_2–0.8%GO. Thus, it was demonstrated that 9% Ce(0.3)–Mn/TiO_2–0.8%GO had better redox performance than 9% Mn/TiO_2–0.8%GO, which was very important for the SCR reaction.

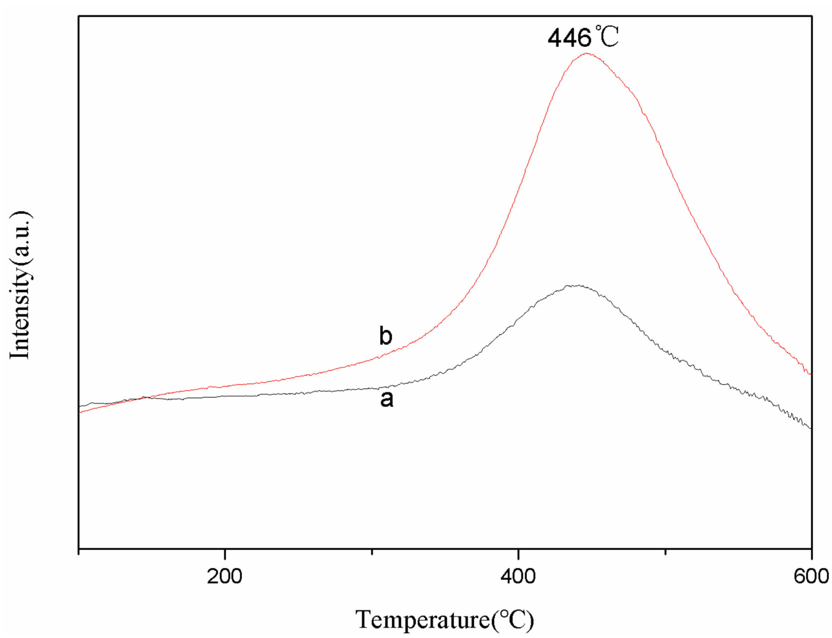

Figure 9. H_2–TPR patterns of 9% Mn/TiO_2–0.8%GO (**a**) and 9% Ce(0.3)–Mn/TiO_2–0.8%GO (**b**).

2.6. Stability Test of the Catalyst

Stability of the 9% Ce(0.3)–Mn/TiO_2–0.8%GO catalyst at 180 °C is shown in Figure 10. The NO_x conversion slightly decreased during the first 30 h and then reached a stable level of about 94%. The NO_x conversion of 94% could last for more than 40 h. Therefore, the 9% Ce(0.3)–Mn/TiO_2–0.8%GO catalyst presented good stability and high SCR activity.

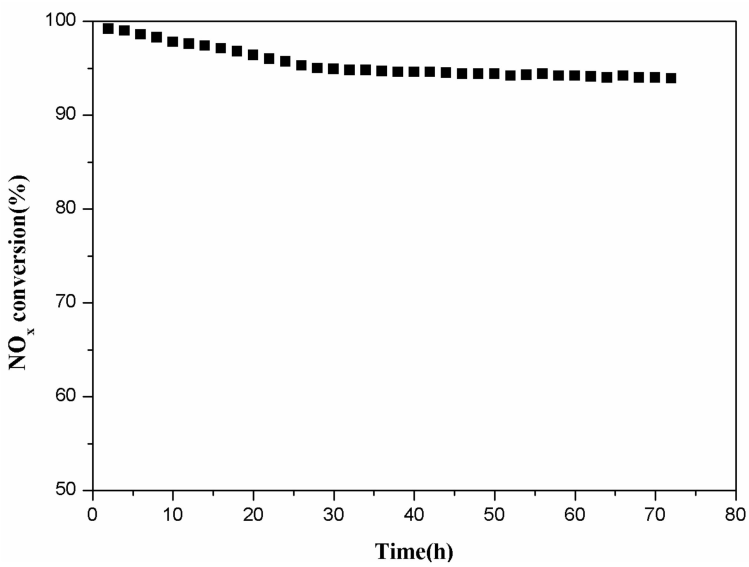

Figure 10. Stability test of 9% Ce(0.3)–Mn/TiO_2–0.8%GO catalyst within 72 h.

3. Materials and Methods

3.1. Synthesis of the Catalyst

Graphene oxide (GO) was synthesized by the modified Hummers method [64]. Firstly, 1 g graphite powder (3000 mesh) and 0.5 g $NaNO_3$ were added into 23 mL of concentrated H_2SO_4 slowly in a 1000 mL beaker in an ice bath with stirring. After being stirred for 10 min, 3 g $KMnO_4$ was added to the mixture, slowly, and the temperature was kept at 35 ± 3 °C for 30 min. Then a certain amount of H_2O_2 (30 wt %) and 46 mL of deionized water were added, and the temperature was maintained at 90 °C for 15 min, and warm deionized water was added to a volume of 140 mL. Then the mixture was filtered and washed with 150 mL diluted HCl (10 wt %) and 500 mL of deionized water three times. Then the obtained graphite oxide was dispersed into 500 mL water by ultrasonication at room temperature for 1 h. Unexfoliated graphite oxide in the suspension was removed by subsequent centrifugation at 4000 rpm for 30 min. The graphene oxide was finally dried at 80 °C for 24 h in a vacuum oven.

TiO_2–0.8 wt %GO nanocomposites were prepared by the sol-gel method. First, GO was dissolved in a certain amount of deionized water by ultrasonic treatment for 1 h. A certain volume of tetrabutyl titanate and ethanol were stirred to obtain solution A. Glacial acetic acid, GO solution, and anhydrous ethanol were dissolved to obtain solution B. Solution B was slowly dropped into solution A, under vigorous stirring, for 90 min to achieve a uniform brown transparent titanium–GO sol. Brown crystals were obtained after aging of this sol at room temperature for 24 h and then drying at a constant temperature of 80 °C for 12 h to remove the organic solution. Finally, the support was ground, calcined in a tubular furnace in a nitrogen atmosphere, and kept warm at 450 °C for 6 h to obtain the TiO_2–0.8%GO powder.

CeO_x–MnO_x/TiO_2–GO catalysts were synthesized with different Mn and Ce loadings totaling 9 wt % by the ultrasonic impregnation method. Manganese acetate and cerium nitrate were chosen as the precursors of the active components. According to the molar ratio of Ce/Mn, certain amount of manganese acetate and cerium nitrate were dissolved in deionized water and added into a breaker containing TiO_2–GO. The mixture was sonicated at 60 °C for 90 min to ensure the dispersion of TiO_2–GO and full contact of the active components with the support. The samples were air-dried at 80 °C for 12 h and then calcined in a tubular furnace in an atmosphere of nitrogen at 450 °C for 6 h. The fin catalysts were denoted as 9 wt % CeO_x(Y)–MnO_x/TiO_2–GO, where Y represents the molar ratio of Ce/Mn.

3.2. Catalyst Characterization

The morphology of the support of the catalysts was observed by FESEM (Hitachi S–4800, Tokyo, Japan). The HRTEM (FEI Tecnai G2 F20, Hillsboro, OR, USA) was used to observe the morphologies and interplanar crystal spacing of the CeO_x–MnO_x/TiO_2–GO catalysts. The specific surface area, pore volume, and pore size of the samples were determined on a Quadrasorb SI-MP surface area analyzer (Quantachrome Instrument, Boynton Beach, FL, USA) with a nitrogen adsorption-desorption method. XPS (Axis Ultra DLD, Kratos Analytical Ltd., Manchester, UK) was used to analyze the chemical state and surface composition of samples. H_2 temperature-programmed reduction (H_2–TPR) and NH_3 temperature-programmed desorption (NH_3–TPD) were performed on a Builder PCA–1200 auto-adsorption apparatus (Builder, Beijing, China). Prior to the H_2–TPR experiment, 100 mg of catalysts were pretreated with N_2 with a total flow rate of 30 mL·min^{-1} at 300 °C for 0.5 h, then cooled to room temperature in an N_2 atmosphere. Finally, the temperature was raised to 600 °C with a constant heating rate of 10 °C·min^{-1} in a flow of H_2 (5 vol %)/N_2 (30 mL·min^{-1}). Prior to the NH_3–TPD experiment, the catalysts (50 mg) were pretreated at 300 °C in a flow of N_2 (30 mL·min^{-1}) for 0.5 h and cooled to 100 °C under N_2 flow. Then the samples were exposed to a flow of NH_3 at 100 °C for 1 h, followed by N_2 purging for 0.5 h. Finally, the reactor temperature was raised to 800 °C under N_2 flow at a constant rate of 10 °C·min^{-1}. The effects of H_2O and SO_2 were analyzed by a Fourier transform infrared spectrometer (FT–IR PROTÉGÉ 460, Thermo Nicolet, Madison, WI, USA).

3.3. Catalyst Activity Test

Steady-state SCR reaction experiments were performed in a quartz tube fixed-bed continuous flow reactor using 500 mg catalyst of 60–100 mesh. The reactor was placed in an electrically-heated furnace with a programmable controller. The typical reactant gas composition included 500 ppm NO, 500 ppm NH_3, 7 vol % O_2, 10 vol % H_2O (when used), 200 ppm SO_2 (when used), with the balance being Ar. The Ar flow gas was divided into two branches. One branch converged with NO, NH_3, O_2, and SO_2 to form the main gas flow, while the other one passed through a heated gas-wash bottle containing deionized water (80 °C) to introduce water vapor into the system when required. The feed flow rate was fixed at 600 mL/min, which was controlled by a mass flow controller and corresponded to a gas hourly space velocity (GHSV) of 67,000 h^{-1}, and the reaction temperature ranged from 80 to 180 °C. At each temperature point, the reaction came to a steady state around 30 min, at which time the experimental data were collected.

NO and NO_2 concentrations at the inlet and outlet were monitored by an NO_x analyzer (42i–HL, Thermo Scientific Ins., Waltham, MA, USA), while the N_2 product was monitored by a gas chromatograph (GC-7890A, Agilent Technologies, Santa Clara, CA, USA). The effluent gas concentrations of N_2O was monitored by a Fourier transform infrared spectrometer (FT–IR PROTÉGÉ 460, Thermo Nicolet, Madison, WI, USA).

The NO_x removal efficiency and the N_2 selectivity were obtained by the following equations:

$$\mathrm{NO_x\ conversion}(\%) = \frac{C^{in}_{NO_x} - C^{out}_{NO_x}}{C^{in}_{NO_x}} \times 100 \tag{1}$$

$$\mathrm{N_2\ selectivity}(\%) = \frac{C^{in}_{NO} + C^{in}_{NH_3} - C^{out}_{NO_2} - 2C_{N_2O}}{C^{in}_{NO} - C^{in}_{NH_3}} \times 100 \tag{2}$$

where $C^{in}_{NO_x}$, C^{in}_{NO}, and $C^{in}_{NH_3}$ correspond to the inlet concentration of NO_x, NO, and NH_3, respectively. $C^{out}_{NO_x}$ and $C^{out}_{NO_2}$ correspond to the outlet concentration of NO_x and NO_2, respectively. C_{N_2O} is the outlet concentration of N_2O.

4. Conclusions

In this paper, a series of 9%CeO_x–MnO_x/TiO_2–GO nanocomposites with different molar ratios of Ce/Mn were synthesized by the sol-gel and ultrasonic impregnation methods. The results showed that the TiO_2–0.8%GO was an ideal support for the catalyst and several valences of manganese and cerium oxides were uniformly distributed on its surface. MnO_x was characterized as MnO, MnO_2, Mn_2O_3, and non-stoichiometric MnO_x/Mn, while CeO_x was characterized as Ce^{4+}, Ce^{3+}, and Ce^{2+} in the samples. The coexistence of various valences of cerium and manganese oxide can improve the redox performance of the catalyst. With the addition of Ce, the amount of MnO_2 and non-stoichiometric MnO_x/Mn, the total oxygen and chemisorbed oxygen content, and the electron transfer ability of the catalyst increased significantly. As a result, the catalyst, with an introduction of Ce in certain amounts, exhibited high catalytic activity and N_2 selectivity at low temperature. When the molar of Ce/Mn was kept at 0.3, the 9%Ce(0.3)–Mn/TiO2-0.8%GO catalyst had the highest SCR activity (more than 99% at 180 °C) and reasonable N_2 selectivity. The catalyst exhibited good resistance to H_2O and SO_2. For the presence of hydrophilic groups on the surface of the GO sheets, the competitive adsorption between H_2O and NH_3 occurred easily, which was considered as the critical factor influencing the H_2O resistance of the catalyst. Due to the pre-sulfuring process of GO, serious sulfation of the active component can be prevented and the catalyst exhibited excellent SO_2 resistance.

Acknowledgments: The authors gratefully acknowledge the Open Foundation of State Key Laboratory of Advanced Metallurgy under grant KF14-09 and Beijing Municipal Science and Technology Project under grant Z161100002716015 for financial support.

Author Contributions: Zhensong Tong and Xining Lu conceived and designed the experiments; Xining Lu performed the experiments; Zhensong Tong and Xining Lu analyzed the data; Zhensong Tong wrote the paper. Cunyi Song provided manuscript editing.

Conflicts of Interest: The authors declare no conflict of interest.

References

1. Kim, C.H.; Qi, G.S.; Dahlberg, K.; Li, W. Strontium-doped perovskites rival platinum catalysts for treating NO_x in simulated diesel exhaust. *Science* **2010**, *327*, 1624–1627. [CrossRef] [PubMed]
2. Parks, J.E. Less costly catalysts for controlling engine emissions. *Science* **2010**, *327*, 1584–1585. [CrossRef] [PubMed]
3. Liu, C.; Shi, J.W.; Gao, C.; Niu, C.M. Manganese oxide-based catalysts for low-temperature selective catalytic reduction of NO_x with NH_3: A review. *Appl. Catal. A* **2016**, *522*, 54–69. [CrossRef]
4. Wang, J.H.; Zhao, H.W.; Haller, G.; Li, Y.D. Recent advances in the selective catalytic reduction of NO_x with NH_3 on Cu-Chabazite catalysts. *Appl. Catal. B* **2017**, *202*, 346–354. [CrossRef]
5. Kwak, J.H.; Tonkyn, R.G.; Kim, D.H.; Szanyi, J.; Peden, C.H.F. Excellent activity and selectivity of Cu-SSZ-13 in the selective catalytic reduction of NO_x with NH_3. *J. Catal.* **2010**, *275*, 187–190. [CrossRef]
6. Xu, W.Q.; Yu, Y.B.; Zhang, C.B.; He, H. Selective catalytic reduction of NO by NH_3 over a Ce/TiO_2 catalyst. *Catal. Commun.* **2008**, *9*, 1453–1457. [CrossRef]
7. Kang, M.; Yeon, T.H.; Park, E.D.; Yie, J.E.; Kim, J.M. Novel MnO_x catalysts for NO reduction at low temperature with ammonia. *Catal. Lett.* **2006**, *106*, 77–80. [CrossRef]
8. Kang, M.; Park, E.D.; Kim, J.M.; Yie, J.E. Manganese oxide catalysts for NO_x reduction with NH_3 at low temperatures. *Appl. Catal. A* **2007**, *327*, 261–269. [CrossRef]
9. Tian, W.; Yang, H.S.; Fan, X.Y.; Zhang, X.B. Catalytic reduction of NO_x with NH_3 over different-shaped MnO_2 at low temperature. *J. Hazard. Mater.* **2011**, *188*, 105–109. [CrossRef] [PubMed]
10. Tang, X.F.; Li, J.H.; Sun, L.A.; Hao, J.M. Origination of N_2O from NO reduction by NH_3 over beta-MnO_2 and alpha-Mn_2O_3. *Appl. Catal. B* **2010**, *99*, 156–162. [CrossRef]
11. Wu, Z.B.; Jin, R.B.; Liu, Y.; Wang, H.Q. Ceria modified MnO_x/TiO_2 as a superior catalyst for NO reduction with NH_3 at low-temperature. *Catal. Commun.* **2008**, *9*, 2217–2220. [CrossRef]
12. Huang, H.Y.; Yang, R.T. Removal of NO by reversible adsorption on Fe-Mn based transition metal oxides. *Langmuir* **2001**, *17*, 4997–5003. [CrossRef]

13. Lian, Z.H.; Liu, F.D.; He, H.; Shi, X.Y.; Mo, J.S.; Wu, Z.B. Manganese-niobium mixed oxide catalyst for the selective catalytic reduction of NO_x with NH_3 at low temperatures. *Chem. Eng. J.* **2014**, *250*, 390–398. [CrossRef]
14. Chang, H.Z.; Chen, X.Y.; Li, J.H.; Ma, L.; Wang, C.Z.; Liu, C.X.; Schwank, J.W.; Hao, J.M. Improvement of activity and SO_2 tolerance of Sn-modified MnO_x-CeO_2 catalysts for NH_3-SCR at low temperatures. *Environ. Sci. Technol.* **2013**, *47*, 5294–5301. [CrossRef] [PubMed]
15. Zuo, J.L.; Chen, Z.H.; Wang, F.R.; Yu, Y.H.; Wang, L.F.; Li, X.H. Low-temperature selective catalytic reduction of NO_x with NH_3 over novel Mn-Zr mixed oxide catalysts. *Ind. Eng. Chem. Res.* **2014**, *53*, 2647–2655. [CrossRef]
16. Liu, Z.M.; Yi, Y.; Zhang, S.X.; Zhu, T.L.; Zhu, J.Z.; Wang, J.G. Selective catalytic reduction of NO_x with NH_3 over Mn-Ce mixed oxide catalyst at low temperatures. *Catal. Today* **2013**, *216*, 76–81. [CrossRef]
17. Wei, Y.J.; Sun, Y.; Su, W.; Liu, J. MnO_2 doped CeO_2 with tailored 3-D channels exhibits excellent performance for NH_3-SCR of NO. *RSC Adv.* **2015**, *5*, 26231–26235. [CrossRef]
18. Jampaiah, D.; Tur, K.M.; Venkataswamy, P.; Ippolito, S.J.; Sabri, Y.M.; Tardio, J.; Bhargava, S.K.; Reddy, B.M. Catalytic oxidation and adsorption of elemental mercury over nanostructured CeO_2-MnO_x catalyst. *RSC Adv.* **2015**, *5*, 30331–30341. [CrossRef]
19. Wang, Y.L.; Ge, C.Z.; Zhan, L.; Li, C.; Qiao, W.M.; Ling, L.C. MnO_x-CeO_2/activated carbon honeycomb catalyst for selective catalytic reduction of NO with NH_3 at low temperatures. *Ind. Eng. Chem. Res.* **2012**, *51*, 11667–11673. [CrossRef]
20. Qi, G.S.; Yang, R.T.; Chang, R. MnO_x-CeO_2 mixed oxides prepared by co-precipitation for selective catalytic reduction of NO with NH_3 at low temperatures. *Appl. Catal. B* **2004**, *51*, 93–106. [CrossRef]
21. Qi, G.S.; Yang, R.T. Performance and kinetics study for low-temperature SCR of NO with NH_3 over MnO_x-CeO_2 catalyst. *J. Catal.* **2003**, *217*, 434–441. [CrossRef]
22. Jin, R.B.; Liu, Y.; Wang, Y.; Cen, W.L.; Wu, Z.B.; Wang, H.Q.; Weng, X.L. The role of cerium in the improved SO_2 tolerance for NO reduction with NH_3 over Mn-Ce/TiO_2 catalyst at low temperature. *Appl. Catal. B* **2014**, *148*, 582–588. [CrossRef]
23. Wu, Z.B.; Jin, R.B.; Wang, H.Q.; Liu, Y. Effect of ceria doping on SO_2 resistance of Mn/TiO_2 for selective catalytic reduction of NO with NH_3 at low temperature. *Catal. Commun.* **2009**, *10*, 935–939. [CrossRef]
24. Yoshikawa, M.; Yasutake, A.; Mochida, I. Low-temperature selective catalytic reduction of NO_x by metal oxides supported on active carbon fibers. *Appl Catal. A* **1998**, *173*, 239–245. [CrossRef]
25. Tang, X.L.; Hao, J.M.; Yi, H.H.; Li, J.H. Low-temperature SCR of NO with NH_3 over AC/C supported manganese-based monolithic catalysts. *Catal. Today* **2007**, *126*, 406–411. [CrossRef]
26. Pradhan, B.K.; Sandle, N.K. Effect of different oxidizing agent treatments on the surface properties of activated carbons. *Carbon* **1999**, *37*, 1323–1332. [CrossRef]
27. Solís, T.V.; Marbán, G.; Fuertes, A.B. Low-temperature SCR of NO_x with NH_3 over carbon-ceramic supported catalysts. *Appl. Catal. B* **2003**, *46*, 261–271. [CrossRef]
28. Liang, Y.Y.; Li, Y.G.; Wang, H.L.; Zhou, J.G.; Wang, J.; Regier, T.; Dai, H.J. Co_3O_4 nanocrystals on graphene as a synergistic catalyst for oxygen reduction reaction. *Nat. Mater.* **2011**, *10*, 780–786. [CrossRef] [PubMed]
29. Pyun, J. Graphene Oxide as Catalyst: Application of carbon materials beyond nanotechnology. *Angew. Chem., Int. Ed.* **2011**, *50*, 46–48. [CrossRef] [PubMed]
30. Cai, S.X.; Hu, H.; Li, H.R.; Shi, L.Y.; Zhang, D.S. Design of multi-shell Fe_2O_3@MnOx@CNTs for the selective catalytic reduction of NO with NH_3: Improvement of catalytic activity and SO_2 tolerance. *Nanoscale* **2016**, *8*, 3588–3598. [CrossRef] [PubMed]
31. Chen, J.H.; Cao, F.F.; Qu, R.Y.; Gao, X.; Cen, K.F. Bimetallic cerium-copper nanoparticles embedded in ordered mesoporous carbons as effective catalysts for the selective catalytic reduction of NO with NH_3. *J. Colloid. Interface Sci.* **2015**, *456*, 66–75. [CrossRef] [PubMed]
32. Cao, F.F.; Chen, J.H.; Lyu, C.L.; Ni, M.J.; Gao, X.; Cen, K.F. Synthesis, characterization and catalytic performances of Cu- and Mn-containing ordered mesoporous carbons for the selective catalytic reduction of NO with NH_3. *Catal. Sci. Technol.* **2015**, *5*, 1267–1279. [CrossRef]
33. Lerf, A.; Heyong, H.; Forster, M.; Klinowski, J. Structure of graphite oxide revisited. *J. Phys. Chem. B* **1998**, *102*, 4477–4482. [CrossRef]
34. Nie, R.F.; Wang, J.H.; Wang, L.N.; Qin, Y.; Chen, P.; Hou, Z.Y. Platinum supported on reduced graphene oxide as a catalyst for hydrogenation of nitroarenes. *Carbon* **2012**, *50*, 586–596. [CrossRef]

35. Li, D.; Kaner, R.B. Materials science-Graphene-based materials. *Science* **2008**, *320*, 1170–1171. [CrossRef] [PubMed]
36. Scheuermann, G. M.; Rumi, L.; Steurer, P.; Bannwarth, W.; Mulhaupt, R. Palladium nanoparticles on graphite oxide and its functionalized graphene derivatives as highly active catalysts for the Suzuki-Miyaura coupling reaction. *J. Am. Chem. Soc.* **2009**, *131*, 8262–8270. [CrossRef] [PubMed]
37. Park, S.; Ruoff, R.S. Chemical methods for the production of graphenes. *Nat. Nanotechnol.* **2009**, *4*, 217–224. [CrossRef]
38. Gao, Y.J.; Ma, D.; Wang, C.L.; Guan, J.; Bao, X.H. Reduced graphene oxide as a catalyst for hydrogenation of nitrobenzene at room temperature. *Catal. Commun.* **2011**, *47*, 2432–2434. [CrossRef] [PubMed]
39. Zhu, Z.P.; Su, D.S.; Weinberg, G.; Schlogl, R. Supermolecular self-assembly of graphene sheets: Formation of tube-in-tube nanostructures. *Nano Lett.* **2004**, *4*, 2255–2259. [CrossRef]
40. Erickson, K.; Erni, R.; Lee, Z.; Alem, N.; Gannett, W.; Zettl, A. Determination of the local chemical structure of graphene oxide and reduced graphene oxide. *Adv. Mater.* **2010**, *22*, 4467–4472. [CrossRef] [PubMed]
41. Nie, R.F.; Shi, J.J.; Xia, S.X.; Shen, L.; Chen, P.; Hou, Z.Y.; Xiao, F.S. MnO_2/graphene oxide: A highly active catalyst for amide synthesis from alcohols and ammonia in aqueous media. *J. Mater. Chem.* **2012**, *22*, 18115–18118. [CrossRef]
42. Su, W.; Lu, X.N.; Jia, S.H.; Wang, J.; Ma, H.Z.; Xing, Y. Catalytic reduction of NO_x over TiO_2-graphene oxide supported with MnO_x at low temperature. *Catal. Lett.* **2015**, *145*, 1446–1456. [CrossRef]
43. Lu, X.N.; Song, C.Y.; Jia, S.H.; Tong, Z.S.; Tang, X.L.; Teng, Y.X. Low-temperature selective catalytic reduction of NO_X with NH_3 over cerium and manganese oxides supported on TiO_2-graphene. *Chem. Eng. J.* **2015**, *260*, 776–784. [CrossRef]
44. Qiu, Y.; Liu, B.; Du, J.; Tang, Q.; Liu, Z.H.; Liu, R.L.; Tao, C.Y. The monolithic cordierite supported V_2O_5-MoO_3/TiO_2 catalyst for NH_3-SCR. *Chem. Eng. J.* **2016**, *294*, 264–272. [CrossRef]
45. Lu, P.; Li, C.T.; Zeng, G.M.; He, L.J.; Peng, D.L.; Cui, H.F.; Li, S.H.; Zhai, Y.B. Low temperature selective catalytic reduction of NO by activated carbon fiber loading lanthanum oxide and ceria. *Appl. Catal. B* **2010**, *96*, 157–161. [CrossRef]
46. Planeix, J.M.; Coustel, N.; Coq, B.; Brotons, V.; Kumbhar, P.S.; Dutartre, R.; Geneste, P.; Bernier, P.; Ajayan, P.M. Application of carbon nanotubes as supports in heterogeneous catalysis. *J. Am. Chem. Soc.* **1994**, *116*, 7935–7936. [CrossRef]
47. Kapteijn, F.; Singoredjo, L.; Andreini, A.; Moulijin, J.A. Activity and selectivity of pure manganese oxides in the selective catalytic reduction of nitric oxide with ammonia. *Appl. Catal. B* **1994**, *3*, 173–189. [CrossRef]
48. Lee, J.Y.; Hong, S.H.; Cho, S.P.; Hong, S.C. The study of deNO_x catalyst in low temperature using nano-sized supports. *Curr. Appl. Phys.* **2006**, *6*, 996–1001. [CrossRef]
49. Chen, Z.H.; Yang, Q.; Li, H.; Li, X.H.; Wang, L.F.; Tsang, S.C. Cr-MnO_x mixed-oxide catalysts for selective catalytic reduction of NO_x with NH_3 at low temperature. *J. Catal.* **2010**, *276*, 56–65. [CrossRef]
50. Fang, C.; Zhang, D.S.; Cai, S.X.; Zhang, L.; Huang, L.; Li, H.R.; Maitarad, P.; Shi, L.Y.; Gao, R.H.; Zhang, J.P. Low-temperature selective catalytic reduction of NO with NH_3 over nanoflaky MnO_x on carbon nanotubes in situ prepared via a chemical bath deposition route. *Nanoscale* **2013**, *5*, 9199–9207. [CrossRef] [PubMed]
51. Thirupathi, B.; Smirniotis, P.G. Nickel-doped Mn/TiO_2 as an efficient catalyst for the low-temperature SCR of NO with NH_3: Catalytic evaluation and characterizations. *J. Catal.* **2012**, *288*, 74–83. [CrossRef]
52. Yu, J.; Si, Z.C.; Chen, L.; Wu, X.D.; Weng, D. Selective catalytic reduction of NO_x by ammonia over phosphate-containing $Ce_{0.75}Zr_{0.25}O_2$ solids. *Appl. Catal. B* **2015**, *163*, 223–232. [CrossRef]
53. Yang, S.X.; Zhu, W.P.; Jiang, Z.P.; Chen, Z.X.; Wang, J.B. The surface properties and the activities in catalytic wet air oxidation over CeO_2-TiO_2 catalysts. *Appl. Surf. Sci.* **2006**, *252*, 8499–8505. [CrossRef]
54. Ponce, S.; Pena, M.A.; Fierro, J.L.G. Surface properties and catalytic performance in methane combustion of Sr-substituted lanthanum manganites. *Appl. Catal. B* **2000**, *24*, 193–205. [CrossRef]
55. Xiao, X.; Sheng, Z.Y.; Yang, L.; Dong, F. Low-temperature selective catalytic reduction of NO_x with NH_3 over a manganese and cerium oxide/graphene composite prepared by a hydrothermal method. *Catal. Sci. Technol.* **2016**, *6*, 1507–1514. [CrossRef]
56. Seifvand, N.; Kowsari, E. TiO_2/in-situ reduced GO/functionalized with an IL-Cr complex as a ternary photocatalyst composite for efficient carbon monoxide deterioration from air. *Appl. Catal. B* **2017**, *206*, 184–193. [CrossRef]

57. Omidvar, A.; Jaleh, B.; Nasrollahzadeh, M. Preparation of the GO/Pd nanocomposite and its application for the degradation of organic dyes in water. *J. Colloid. Interface Sci.* **2017**, *496*, 44–50. [CrossRef] [PubMed]
58. Wang, J.H.; Liang, S.; Ma, L.; Ding, S.J.; Yu, X.F.; Zhou, L.; Wang, Q.Q. One-pot synthesis of CdS-reduced graphene oxide 3D composites with enhanced photocatalytic properties. *CrystEngComm* **2014**, *16*, 399–405. [CrossRef]
59. Wang, C.; Sun, L.A.; Cao, Q.Q.; Hu, B.Q.; Huang, Z.W.; Tang, X.F. Surface structure sensitivity of manganese oxides for low-temperature selective catalytic reduction of NO with NH_3. *Appl. Catal. B* **2011**, *101*, 598–605. [CrossRef]
60. Wan, Y.P.; Zhao, W.R.; Tang, Y.; Li, L.; Wang, H.J.; Cui, Y.L.; Gu, J.L.; Li, Y.S.; Shi, J.L. Ni-Mn bi-metal oxide catalysts for the low temperature SCR removal of NO with NH_3. *Appl. Catal. B* **2014**, *148*, 114–122. [CrossRef]
61. Zhan, S.H.; Zhu, D.D.; Qiu, M.Y.; Yu, H.B.; Li, Y. Highly efficient removal of NO with ordered mesoporous manganese oxide at low temperature. *RSC Adv.* **2015**, *5*, 29353–29361. [CrossRef]
62. Yao, X.J.; Kong, T.T.; Yu, S. H.; Li, L.L.; Yang, F.M.; Dong, L. Influence of different supports on the physicochemical properties and denitration performance of the supported Mn-based catalysts for NH_3-SCR at low temperature. *Appl. Surf. Sci.* **2017**, *402*, 208–217. [CrossRef]
63. Deng, J.G.; Zhang, L.; Dai, H.X.; Xia, Y.S.; Jiang, H.Y.; Zhang, H.; He, H. Ultrasound-assisted nanocasting fabrication of ordered mesoporous MnO_2 and Co_3O_4 with high surface areas and polycrystalline walls. *J. Phys. Chem. C* **2010**, *114*, 2694–2700. [CrossRef]
64. Hummers, W.S.; Offerman, R.E. Preparation of graphitic oxide. *J. Am. Chem. Soc.* **1958**, *80*, 1339. [CrossRef]